Narrow equilibrium window for complex coacervation of tau and RNA under cellular conditions

Yanxian Lin[1]*, James McCarty[2]*, Jennifer N. Rauch[3,4], Kris T. Delaney[5], Kenneth S. Kosik[3,4], Glenn H. Fredrickson[5,6], Joan-Emma Shea[2,7], Songi Han[2,6]†

* equal contributions

† corresponding author

1. Biomolecular Science and Engineering, University of California Santa Barbara, Santa Barbara, CA 93106, USA
2. Department of Chemistry and Biochemistry, University of California Santa Barbara, Santa Barbara, CA, 93106, USA
3. Molecular, Cellular and Developmental Biology, University of California Santa Barbara, Santa Barbara, CA 93106, USA
4. Neuroscience Research Institute, University of California Santa Barbara, Santa Barbara, CA 93106, USA
5. Materials Research Laboratory, University of California Santa Barbara, Santa Barbara, CA 93106, USA
6. Department of Chemical Engineering, University of California Santa Barbara, Santa Barbara, CA 93106, USA
7. Department of Physics, University of California Santa Barbara, Santa Barbara, CA 93106, USA

Abstract

The conditions that lead to the liquid-liquid phase separation (LLPS) of the tau protein, a microtubule associated protein whose pathological aggregation has been implicated in neurodegenerative disorders, are not well understood. Establishing a phase diagram that delineates the boundaries of phase co-existence is key to understanding its LLPS. Using a combination of EPR, turbidity measurements, and microscopy, we show that tau and RNA form complex coacervates with lower critical solution temperature (LCST) behavior. The coacervates are reversible, and the biopolymers can be driven to the supernatant phase or coacervate phase by varying the experimental conditions (temperature, salt concentration, tau:RNA charge ratio, total polymer concentration and osmotic stress). Furthermore, the coacervates can be driven to a fibrillar state through the addition of heparin. The equilibrium phase diagram of the tau/RNA complex coacervate system can be described by a Flory-Huggins model, augmented by an approximate Voorn Overbeek electrostatic term (FH-VO), after fitting the experimental data to an empirical Flory interaction parameter divided into an entropic and enthalpic term. However, a more advanced model in which tau and RNA are treated as discrete bead-spring chains with a temperature-dependent excluded volume interaction and electrostatic interactions between charged residues, investigated through field theoretic simulations (FTS), provided direct and unique insight into the thermodynamic driving forces of tau/RNA complexation. FTS corroborated the experimental finding that the complex coacervation of tau and RNA is has an entropy-driven contribution, with a transition temperature around the physiological temperature of 37 °C and salt concentrations around 100-150 mM. Together, experiment and simulation show that LLPS of tau can occur under physiological cellular conditions, but has a narrow equilibrium window over experimentally tunable parameters including temperature, salt and tau

concentrations. Guided by our phase diagram, we show that tau can be driven towards LLPS under *live* cell coculturing conditions with rationally chosen experimental parameters.

Introduction

Protein liquid-liquid phase separation (LLPS) is a process in which proteins assemble and partition into a protein-dense phase and a protein-dilute phase. The proteins in the dense phase form droplets, and retain liquid-like mobility, as shown by NMR measurements [1,2]. The process of LLPS *in vitro* has been observed for decades [3–8], but the field has recently been invigorated by the realization that LLPS also occurs *in vivo*, suggesting a possible physiological role for these assemblies[4,9,10]. The overwhelming majority of proteins observed to undergo LLPS are intrinsically disordered proteins (IDPs) [11], and much of the research thus far has focused on ALS-related IDPs, including FUS [9,12–14], hnRNPA2B1 and hnRNPA1 [15], TDP-43 [15,16], C9ORF72 [17–19] and Ddx4 [20]. Recently, we and others discovered that another amyloid forming IDP, the microtubule binding protein tau, also undergoes LLPS [21–25]. Interestingly, many of the LLPS forming IDPs have been observed to form amyloid fibrils in cell-free systems [13,15], leading to a number of hypotheses regarding the physiological role of LLPS in regulating aggregation. In particular, a compelling idea is that protein LLPS may be an intermediate regulatory state, which could redissolve into a soluble state or transition to irreversible aggregation/amyloid fibrils [13–15,21,22].

In a healthy neuron, tau is bound to microtubules. When tau falls off the microtubule under adverse conditions to the cell, tau is solubilized in the intracellular space as an IDP. Under certain conditions, tau forms intracellular fibrillary tangles, a process linked to neurodegenerative tauopathies that include Alzheimer's disease. In recent work, we showed that

tau in neurons strongly (nanomolar dissociation constant) and selectively associates with smaller RNA species, most notably tRNA [22]. We also found tau and RNA, under charge matching conditions, to undergo LLPS [22] in a process determined to be complex coacervation (CC) [26]. We found that tau-RNA LLPS is reversible, and persisted for > 15 hours without subsequent fibrilization of tau, and hypothesized that LLPS is potentially a physiological and regulatory state of tau.

In this work, we characterize the phase diagram of tau/RNA LLPS using a combination of experiment and simulation, and thereby specify the conditions that drive the system towards a homogeneous phase or an LLPS state. We study a N-terminus truncated version of the longest isoform of human 4R tau *in vitro*, and first demonstrate that tau/RNA complexation is reversible, and that tau remains dynamic and without a persistent structure within the dense phase. The phase coexistence curve separating a supernatant phase from a condensate phase is determined by the system's free energy, which in turn is state dependent, *i.e.* dependent on concentration, temperature, salt, and the nature of the interaction strength between the various solution constituents, including the solvent. We construct the phase diagram from cloud-point measurements of the onset of complex coacervation under varying conditions of temperature, salt, and polymer concentrations. These experiments establish the features and phase coexistence boundaries of the phase diagram, which we then model using theory and simulation to rationalize and understand the physical mechanisms that drive and stabilize LLPS.

A number of theoretical models can be used to model LLPS, each with their own advantages and disadvantages. Ideally, one would turn to simulations at atomic resolution in explicit solvent; however, such models are computationally prohibitive given the multiple orders of magnitude in time and length scales involved in LLPS. Turning to the polymer physics

literature, theoretical treatments of simplified coarse-grained models are much more computationally tractable, and offer useful insight. Although approximate, analytical theories can be formulated, providing an extremely efficient platform for describing the thermodynamics of polyelectrolyte mixtures [27]. These include the Flory-Huggins model [28], the Voorn-Overbeek model [6,29–34], the random-phase approximation [35–37], the Poisson-Boltzmann cell model [38,39], as well as other more sophisticated approaches[40–42], which have been applied to synthetic polymers with low sequence heterogeneity [29,43–46], and to proteins with single composition [2,20,47,48]. While such models have been successful in describing simpler polyelectrolytes, it is less apparent that these models are suitable to describe the complex coacervation of the more complicated tau/RNA system. The simplest approach that one can use is the Flory-Huggins (FH) model, augmented by the Voorn and Overbeek (VO) correction to describe electrostatic correlations. This model is widely used to model LLPS; however, while experimental data can be fit to the model [2,20], ultimately the FH-VO model has serious inadequacies. The original Flory-Huggins model is a mean-field theory, which means that fluctuations in polymer densities away from their average value in each phase are neglected. Augmenting the FH model with a VO treatment of electrostatics approximately accounts for charge correlations, but it entirely neglects chain-connectivity [49]. Thus, the FH-VO model is unable to model the spatially varying charge distribution along the polymer backbone. Ideally, one would like to introduce chain connectivity, charge correlation, and uneven charge distribution into a more realistic polymer physics model; however, a full treatment of polymer density fluctuations is analytically intractable. One possible approach is to pursue a Gaussian approximation to field fluctuations, also known as the random phase approximation (RPA) [50–52]. The RPA model can be viewed as a lowest-order correction to the mean field

126 approximation, and was recently introduced to describe the charge pattern and sequence-
127 dependent LLPS of IDPs [53,54]. The advantage of the RPA model, over the mean-field FH-VO
128 model, is that charge correlations are introduced in a formally consistent manner. Nonetheless, it
129 has been recently demonstrated that the RPA model fails to quantitatively predict polymer
130 concentrations in the dilute phase, given that higher-order fluctuations are important in this
131 regime [55,56].

132 Of all the models described above, fitting experimental data with the FH or FH-VO
133 theory is currently the preferred methodology in the LLPS community to describe and analyze
134 phase diagrams. We demonstrate that this model can be fit to describe our experimental data, but
135 the learning outcome from this modeling is limited. Thus, we take a different approach by
136 computing the exact phase diagram of an off-lattice coarse-grained polyelectrolyte model using
137 field theoretic simulations (FTS). FTS is a numerical approach that allows one to fully account
138 for fluctuations, and thus serves as an approximation-free method to compute equilibrium
139 properties from a suitably chosen coarse-grained representation of the true system. The ability to
140 perform field theoretic simulations enables us to include the important physics of polymer
141 sequence-specificity that cannot be captured by FH-VO, including charge distribution and chain
142 connectivity. Results from FTS are compared to those obtained from the FH-VO model.

143 The model substantiates the experimental phase diagram that the equilibrium window for
144 the complex coacervation of tau and RNA under cellular conditions is narrow. Guided by the
145 phase diagram, empirically obtained from *in vitro* experiments and validated by simulation, we
146 finally show that LLPS of tau-RNA can be established and rationalized under cellular co-
147 culturing conditions in the presence of live cells.

148

149

Results

Tau-RNA complex coacervate is reversible and a dynamic liquid phase.

Truncated versions of the longest isoform of human 4R tau, residues 255-441 [57] and residues 255-368 were used to study tau-RNA complex coacervation (CC). A C291S mutation was introduced to either tau variant, resulting in single-cysteine constructs. Thioflavin T assays and TEM imaging were performed showing these variants retain the capability to form fibrils with morphology similar to full length tau. Unless otherwise specified, we refer to these two single-cysteine tau constructs as tau187 and tau114 (tau114 is close to K18, 244-372 [58]), respectively, while tau refers collectively to any of these variants (see SI methods for experimental details). Importantly, experiments were performed with freshly eluted tau within 30 minutes upon purification to minimize the effects of possible disulfide bond formation. This minimizes the influence of the cysteine mutations on the LLPS behavior of tau-RNA CC. The single-cysteine containing tau187 can be singly spin labeled at site 322, referred to as tau187-SL (see SI methods). Full length tau, tau187 and tau114 are overall positively charged with an estimated +3, +11 and +11 charge per molecule at neutral pH, respectively, based on their primary sequences. The charged residues of tau are more concentrated in the four repeat domains (Fig 1A). PolyU RNA (800~1000 kDa), which is a polyanion carrying 1 negative charge per uracil nucleotide, was used in this study and henceforth referred to as RNA (Fig 1A). Under ambient conditions, both tau and RNA are soluble and stable in solution. By mixing tau and RNA under certain conditions, a turbid and milky suspension was obtained within seconds, where tau and RNA formed polymer-rich droplets (dense phase) separated from polymer-depleted supernatants (dilute phase) (Fig 1B). These polymer-rich droplets are tau-RNA CCs.

We began by determining the concentration of the dense and dilute phases. After mixing and centrifuging 60 μL tau187-RNA droplet suspension, we separated a polymer-rich phase of volume <1 μL with a clear boundary against the dilute supernatant phase. Applying UV-Vis spectroscopy (see SI methods), we determined the concentration of tau and RNA inside the droplets as >76 mg/mL and >17 mg/mL with partitioning factors of >15 and >700 respectively. This is consistent with our previously findings that tau is virtually exclusively partitioned within the dense phase [22]. High protein concentrations are typically correlated with higher propensity for irreversible protein aggregations. In order to verify that there was indeed no fibril formation, tau187-RNA CCs were prepared by mixing tau187-SL and RNA (see SI methods) and monitored by continuous wave electron paramagnetic resonance spectroscopy (For details of cw-EPR experiments see SI methods). The cw-EPR spectra shows no broadening (Fig 1C), and the cw-EPR spectra analysis reveals an unchanged rotational correlation time for the spin label of tau187-SL, τ, of 437 ± 37 ps as a function of time after > 96 hours of incubation at room temperature (Fig 1D, turquoise) (see SI methods). For comparison, cw-EPR spectra and τ were recorded of tau187-SL alone in buffer, and of tau187-SL in the presence of heparin under fibril forming conditions. Tau187-SL alone in buffer showed cw-EPR spectra overlapping with those of tau187-RNA CC, and rotational correlation time τ, 425 ± 16 ps, nearly identical to the τ of tau187-SL CCs (Fig. 1D, red). In contrast, tau187-SL with heparin shows a significantly broadened cw-EPR spectrum and an increasing τ to 2.3 ± 0.7 ns (Fig 1C, D, green). Note that a hundreds of ps range of τ corresponds to rapid tumbling of the spin label, whose rotational degree of freedom is minimally hindered by molecular associations, while a several ns range of τ corresponds to slow tumbling and molecular hindering by association or confinement. The Thioflavin T (ThT) fluorescence curves of the same sample system as a function of time

196 confirms the absence of amyloid aggregate formation in tau187-RNA CCs (Fig S1). These
197 results together suggest that tau187-RNA CCs are in an equilibrium state, in which tau retains its
198 solution-like dynamics.

199 Next, we investigated the reversibility of tau187-RNA complex coacervation. Tau187-RNA
200 CCs were prepared again and incubated by cyclically ramping the temperatures (1 °C/min)
201 upwards and downwards, while the absorbance at λ = 500 nm was monitored, referred to as
202 turbidity hereafter. Ramping rates of 0.5 °C/min and 1 °C/min were tested, but the results shown
203 to be indistinguishable. Microscopy images were concurrently acquired at low and high turbidity,
204 confirming the appearance and abundance of CC droplets correlating with turbidity increase, and
205 *vice versa* (Fig 1E). The turbidity-temperature curves show that at high temperature, samples
206 became turbid with $Abs_{500} \sim 1.5$ and abundance of CCs, while at low temperature, samples
207 became transparent with $Abs_{500} \sim 0$ and absence of CCs. This demonstrates tau187-RNA CC
208 formation is favored at higher temperature, following clearly a lower critical solution
209 temperature behavior (LCST) (Fig 1E) [59]. By cycling the temperature, we robustly and
210 reversibly changed the tau187-RNA mixture between a turbid state to a completely transparent
211 state (Fig 1E). The transition temperatures at which the turbidity emerged during heating and
212 vanished during cooling stay invariant with repeated heating-cooling cycles. The method of
213 extracting a cloud point for the LCST transition temperature from such data will be described in
214 detail in the next section. Importantly, the history of temperature change does not affect the
215 resulting state. Hence the formation and dissolution of tau187-RNA CCs are reversible and
216 consistent with a path-independent equilibrium process. We point out that the maximum
217 turbidity value successively decreases with each heating cycle (Fig 1E), even though the
218 transition temperatures remain invariant. This can be attributed to slow degradation of RNA with

time, (as demonstrated in Fig S2) by verifying an altered turbidity change in the presence of RNase or RNase inhibitor.

It is understood that upon gradual heating of the solution phase, the mechanism of LLPS proceeds via a nucleation process [60], and hence there is a kinetic barrier evidenced by the observed hysteresis in Fig 1E. Nonetheless, we conclude that the final tau-RNA CC state reached upon heating is a true thermodynamic state, and thus can be modeled by an equilibrium theory of phase separation.

Tau-RNA complex coacervate phase diagram

To understand the principles and governing interactions driving tau-RNA CC formation, we constructed a phase diagram for tau187-RNA CC by measuring the transition temperature – to be described in greater detail below – as a function of protein concentration and salt concentration. We first recorded tau187-RNA turbidity at various [tau], [RNA] and [NaCl] values, ranging from 2-240 μM, 6-720 μg/mL and 30-120 mM, respectively. Titrating RNA to tau187, the turbidity was found to be peaked when [RNA]:[tau] reached charge matching condition at which the charge ratio between net positive and negative charges was 1:1 (which for tau187 and RNA used in this study corresponded to [tau187]:[RNA] = 1 μM : 3 μg/mL), validating once more that LLPS is driven by complex coacervation (CC) (Fig S3). Henceforth, all phase diagram data are acquired at a charge matching condition between RNA and tau. Titrating NaCl to tau187-RNA, CC formation showed a steady decrease of turbidity (Fig S3). Combined, these demonstrate that tau187-RNA CC favors the condition of charge balance and low ionic strength, which is consistent with known properties of CC and previous findings [22].

We next investigated the phase separation temperatures under various sample compositions. Tau187-RNA CCs were prepared with a fixed [tau]:[RNA] ratio corresponding to

the condition of net charge balance. Therefore, the composition of tau187-RNA CC can be determined by [tau] and [NaCl]. Samples were heated at 1 °C/min between T = 15-25 °C, while the turbidity was monitored. The turbidity-temperature data of the heating curves were then fit to a sigmoidal function, so that the cloud point temperature, T_{cp}, could be extracted as shown in Fig 2A (T_{cp} was determined from heating curves out of practical utility; T_{cp} from cooling curves is possibly closer to thermodynamic transitions). The experimental cloud-point temperature T_{cp} for CC formation as a function of [tau] and [NaCl] are shown (as points) in Fig 2B and Fig 2C. The experimental data points show that increasing [tau] lowers T_{cp}, favoring CC formation, while increasing [NaCl] raises T_{cp}, disfavoring CC formation. Such trends were observed at two [NaCl] and two [tau] values, respectively (Fig 2B, 2C). Experimentally, T_{cp} was determined for a range of [tau] and [NaCl] conditions (see Fig S4).

The features of the Tau-RNA CC phase diagram were also investigated by comparing tau187 and tau114. Tau187-RNA CC and tau114-RNA CC were prepared with 20 μM tau187 and 28 μM tau114, so that the total concentration of polymer, i.e. tau and RNA, reaches 0.5 mg/mL. Turbidity was recorded at varying [NaCl]. Similar to the observation with tau187-RNA CC, tau114-RNA CC showed decreasing turbidity at increasing [NaCl] (Fig S5). The [NaCl] values where turbidity reaches 0 were estimated as 131 mM and 150 mM for tau187 and tau114, respectively, implying CC formation is more favorable with tau114 that hence can sustain higher [NaCl]. Based on this, 20 μM of tau187, 131 mM of NaCl and room temperature, 20 °C, were used as the phase separation conditions ([tau], [NaCl] and T_{cp}) for tau187, and 28 μM, 150 mM and 20 °C for tau114. These two experimental conditions were used in the next section for comparing the two constructs of tau.

Flory-Huggins-Voorn-Overbeek Fit to Experimental Phase Diagram

We next used the FH-VO model to fit the experimental data for the tau187-RNA CC system, as is commonly done in LLPS studies. Despite its theoretical deficiencies the FH-VO model is commonly used for its simplicity and ease of implementation. Our system consists of five species: tau187, RNA, monovalent cation (Na^+), anion (Cl^-) and water. For simplicity, we explicitly consider only the effect of excess salt, and do not include polymer counterions. The FH-VO model maps these five species onto a three-dimensional lattice (Fig 2D). Each polymer is treated as a uniform chain with degree of polymerization N and average charge per monomer σ. N was taken as the average chain length of the species (1 for monovalent ions). The charge density σ of RNA, monovalent ions and water were set to 1, 1 and 0 respectively. The values for σ of tau187 or tau114 were calculated from the net charge at neutral pH divided by the chain length. The composition of the species is expressed in terms of the volume fraction ϕ of the occupied lattice sites, which are proportional to the molar concentrations (see SI methods for details). As in experiments, tau187-RNA CCs were prepared at fixed [tau]:[RNA] and $[Na^+]$:$[Cl^-]$ ratios. Under these two constraints, the volume fraction of all five species in tau187-RNA CC listed above can be determined with two variables, [tau] and [NaCl], which are experimentally measurable.

Given N, σ, [tau], [NaCl] and T_{cp}, the task is to find ϕ_{tau}^{I} and ϕ_{tau}^{II}, the volume fractions of tau in the dilute and dense, coacervate, phase at equilibrium, i.e. the binodal coexistence points. The model and procedure is described in detail in the SI methods. For each experimental observation of T_{cp} determined for a given [tau] and [NaCl] (Fig S4), the FH-VO expression has one unknown parameter, the Flory-Huggins χ term. The Flory-Huggins χ parameter is introduced as an energetic cost to having an adjacent lattice site to a polymer segment occupied by a solvent

molecule [61]. Here we take χ to be an adjustable parameter, such that given a suitable expression for χ, the complete binodal curve can be modeled with the FH-VO theory. Consequently, we first solved for χ at each given experimental condition, so that the theoretical binodal curve intersects the experimental data point. Fig 2E shows two representative examples of a theoretical binodal curve (solid line) intersecting a single experimental data point at the given [NaCl] and [tau]. This procedure gives an empirical χ parameter for each experimental data point, as collated in Fig 2F as a function of 1/ T_{cp}. We then performed to this set of experimental data a least-squares fit of the empirical χ parameter to the form A + B/T (Fig 2F), yielding an expression of the temperature dependence of χ of

$$\chi\,(T) = 1.8 - \frac{390}{T},\ R^2 = 0.67. \qquad \text{(Equation 1)}$$

Finally, from this expression for χ(T), we computed the binodal curves that establishes the phase coexistence as a function of T_{cp}, [tau] and [NaCl], shown as solid lines, only for the dilute phase coexistence for T_{cp} vs [tau] (Fig 2B) and T_{cp} vs [NaCl] (Fig 2C). For the full phase diagram showing both dilute and dense binodal curves see Fig. S7. The experimental data (shown as points) and computed binodal curves both exhibited a decreasing T_{cp} with increasing [tau] and an increasing T_{cp} with increasing [NaCl]. This simply establishes that tau-RNA CC favors higher tau concentrations in the 1-240 μM range and lower ionic strength in the 30-120 mM range tested here. Binodal curves for tau114-RNA CC were also computed, and are compared with tau187-RNA CC, along with experimental data (Fig. S5). Comparison of the two constructs shows that tau114-RNA CC has a lower T_{cp} than tau187-RNA CC, suggesting it is more favorable to phase separation. This qualitatively agrees with experimental observations. Note that the experimental conditions are for [tau] and [RNA] set at charge matching conditions for maximal CC, and thus [tau] and [RNA] are locked relative to each other. When [RNA] falls

311 either well below or well above charge matching condition relative to [tau], it is expected that the
312 LLPS envelope will collapse.
313
314 **Field theoretic simulations of a coarse-grained model of tau-RNA complex**
315 **coacervation**
316
317 Although the FH-VO model can be brought into agreement with experiment through a judicious
318 choice of χ, it is fundamentally unsound from a theoretical perspective, noticeably because it
319 neglects connectivity between charges on the same chain. This is a severe limitation because it is
320 expected that subtle difference in primary amino acid sequences may have a profound effect on
321 the phase diagram. A particularly appealing alternative to gain insights into the thermodynamics
322 of LLPS is to perform field theoretic simulations (FTS) on a physically motivated polyelectrolyte
323 model (Fig 3), in which each amino acid is represented by a single monomeric unit of length *b* in
324 a coarse-grained bead-spring polymer model. The charge of each segment is unambiguously
325 assigned from the particular amino acid charge at pH 7.0. In addition to harmonic bonds between
326 nearest neighbors, which enforces chain connectivity, all segment pairs interact via two types of
327 non-bonded potentials: a short-ranged excluded volume repulsion and a long-range electrostatic
328 interaction between charged monomers (see Fig 3). We take the polymers to be in a slightly good
329 solvent, meaning that favorable interactions between monomers and solvent cause chain
330 swelling. In such cases, the excluded volume interaction is modeled as a repulsive Gaussian
331 function between all monomer pairs with a strength that increases with solvent quality [62].
332 Conversely, as solvent quality decreases, the excluded volume repulsion decreases, approaching
333 zero at the so-called theta condition. In the present case we limit ourselves to the case where the
334 excluded volume is positive and small, i.e. a good solvent near the theta condition. Simulations

335 are performed using a single excluded volume strength, v, identical for all monomers, which is
336 an input parameter in the model and can be adjusted to parameterize the favorable monomer-
337 solvent interactions. Additionally, the long-range electrostatic interactions are described by a
338 Coulomb potential in a screened, uniform, dielectric background. The length scale of the
339 electrostatic interactions is parameterized by the Bjerrum length l_B, which is the distance at
340 which the electrostatic interactions become comparable to the thermal energy k_BT and is defined
341 as

342 $$l_B = \frac{e^2}{4\pi\epsilon_0\epsilon_r k_B T} \qquad \text{(Equation 2)}$$

343 where e is the unit of electronic charge, ϵ_r the dielectric constant ($\epsilon_r = 80$ for water), and ϵ_0
344 the vacuum permittivity.

345 The main features of the model used for FTS here are the inclusion of chain connectivity,
346 charge sequence-dependence for the electrostatic interactions based on the primary amino acid
347 sequence of tau, solvation effects which are parameterized by the single excluded volume
348 parameter, v, and an electrostatic strength parameterized by the Bjerrum length, l_B. FTS is
349 performed in implicit solvent with a uniform dielectric background. We assume that the polymer
350 chains are in a fully dissociated state, and we do not explicitly represent counter ions. The effect
351 of excess salt is included in our model by introducing point charges explicitly, which engage in
352 Coulomb interactions with all other charged species and repel other ions and polymer segments
353 at short distances by the same Gaussian excluded volume repulsion. By introducing explicit
354 small ions in this manner, we are neglecting strong correlations such as counter ion
355 condensation; however, we are allowing for weak correlations of the Debye-Hückel type. The
356 explicit addition of salt will serve to screen the electrostatic interactions and inhibit the driving
357 force for CC, in agreement with the experiments.

Details of the FTS protocol are described in the SI methods. By performing FTS at various state points and computing equilibrium properties, we first set out to fully explore the parameter space relevant for LLPS in this model. This involves running simulations at different conditions analogous to experiments. For each simulation the thermodynamic state of the system is determined by specifying a particular value for the dimensionless excluded volume parameter v/b^3, the dimensionless Bjerrum length l_B/b, and the dimensionless monomer number density ρb^3. Fig 4 shows the final polymer density configuration for two representative simulations at a monomer density of $\rho b^3 = 0.22$ at different thermodynamic conditions (see caption for Fig 4 for details). Although the bulk density is fixed and identical for the two cases, the local polymer density is free to fluctuate. The left simulation box (Fig 4) shows a case where a single phase is favored, indicated by a nearly homogenous polymer density throughout the simulation box (white/blue). This is contrasted by the right simulation box (Fig 4) depicting the case where the system phase separates into a dilute polymer-deplete region (white) and a dense polymer-rich droplet region (red)—the coacervate phase with the color signifying the polymer density. Fig 4 shows that given suitable parameterization, FTS can be used to study complex coacervation of a coarse-grained tau-RNA model. Given this observation, we next map out the full phase diagram in the parameter space of the model while fixing the physical parameters of charge sequence, chain length, and chain volume fractions that are consistent with the experimental conditions.

Field theoretic simulations predict phase equilibria around physiological conditions

The parameters to be explored in connection with phase behavior are the strength of the interactions in the polyelectrolyte model: the excluded volume strength v and the Bjerrum length l_B. A direct comparison between FTS and the experimental phase diagram will be deferred until the following section. The phase coexistence points (binodal conditions) for a given value of the

382 excluded volume v and Bjerrum length l_B can be obtained by running many simulations over a
383 range of concentrations, and finding the concentration values at which the chemical potential and
384 the osmotic pressure are equal in both phases (see Fig. S10). The procedure is described in the
385 SI, and is repeated for many different v and l_B combinations. The resulting phase diagram will be
386 a three-dimensional surface which is a function of ρ, v, and l_B. In Fig 5A, we show a slice of this
387 surface along the $l_B - \rho$ plane with a fixed value of $v = 0.0068\, b^3$, and in Fig 5B we show a
388 slice along the $v - \rho$ plane with a fixed $l_B = 1.79\, b$ (at $T = 293$ K, Eq. 3). It should be noted that
389 Fig 5 presents the first approximation-free phase diagrams presented in the literature of a
390 theoretical model describing a biological complex coacervate system. From Fig 5, one can see
391 that l_B and v have counteracting effects, namely increasing v that is caused by increased solvent
392 quality destabilizes the coacervate phase and favors the single phase, whereas increasing l_B that
393 is caused by reduced electrostatic screening favors coacervation, and destabilizes the single
394 phase. The physical interpretation of the trends in Fig 5 is that the actual binodal for the
395 experimental system will depend on two competing features: the solvent quality proportional to
396 v, which inhibits coacervation, and the electrostatic strength of the media proportional to l_B
397 which promotes coacervation.

398 The FTS- derived phase diagram shown in Fig 5 provides a guide how to experimentally tune
399 the window for complex coacervation by changing the relative contribution of the solvent quality
400 or the dielectric strength. Experimentally, the solvent quality can be decreased by adding
401 crowding agents or by changing the hydrophilic/hydrophobic amino acid composition, while the
402 electrostatic strength can be controlled by the salt concentration. Increasing salt concentration
403 tends to decrease the bare electrostatic strength by screening the charges, and this is predicted to

stabilize the single phase solution mixture against coacervation, in agreement with experimental observation. We explore these ideas further below in the context of tau coacervation *in vivo*.

Despite the simplicity of the coarse-grained description, the model predicts that these two competing parameters, excluded volume vs. electrostatic interactions, are nearly balanced around physiological salt concentration, temperature, and protein concentration. Assuming that the relative dielectric constant for water is $\epsilon_r = 80$, and that the segment size b is approximately equivalent to the distance between C_α carbons, i.e. b ~4 Å, it follows that $l_B = 1.75b$ at 300 K. ($l_B = 0.7\,nm$ at 300 K). In the $l_B - \rho$ plane (shown in Figure 5A), at the cross section of $l_B = 1.75$, three points for ρb^3 are indicated that correspond to 1, 5, and 10 μM for tau concentrations at 300 K. Here we have implicitly assumed that at physiological temperature and in a crowded cellular environment tau is near the theta condition, and thus v is small. This analysis suggests that small modulation in the experimental conditions, such as changes in the temperature or salt concentration, local pH or crowding effects (via the excluded volume parameter v) can readily and reversibly induce complex coacervation *in vivo* under physiological conditions.

Comparison between simulation and experiment

In the preceding section we presented the phase diagram from FTS explicitly in terms of the model parameters of the excluded volume v and Bjerrum length l_B. We now seek to compare our simulation results directly with the experimental phase diagram. This requires knowing precisely how the model parameters depend on temperature. We again take the monomer size b to be approximately the distance between the C_α carbons b ~4 Å, and assume a dielectric constant of $\epsilon_w = 80$ for pure water. The relative dielectric ϵ_r at a given salt concentration is then estimated

from Equation 2. With these values, the Bjerrum length l_B can be estimated from Equation 3 at the experimental cloud point temperature (Fig 6A), which leaves only one unknown parameter v.

The excluded volume is typically taken to be proportional to $(1 - \theta/T)$ where θ is the theta temperature, the temperature at which the chain follows ideal chain statistics [62–64]. For LCST behavior it is customary to introduce the form $v = -v_0(1 - \theta/T)$ where v_0 controls the magnitude of the excluded volume interactions [65]. This form of the excluded volume implies that at temperatures lower than the theta temperature, the excluded volume is repulsive ($v > 0$, meaning a good solvent) and for temperatures above the theta point, the excluded volume becomes attractive ($v < 0$, poor solvent conditions). By adjusting the excluded volume in FTS to fit a subset of the experimental data, (shown in Fig. 6B), we then perform a linear fit to obtain a value of $v_0 = 0.25b^3$ and $\theta = 309$ K. Note that in the range of temperatures considered, the excluded volume remains positive. However, for temperatures higher than θ, when the excluded volume becomes negative, the polymer chain will collapse, consistent with the observation in the literature [66], which showed that tau undergoes a thermal compaction at high temperatures due to entropic factors [63]. In such high temperature regimes a more sophisticated treatment is needed; however, all our experimental conditions remain below this threshold. Having mapped the two model parameters v and l_B to the experimental temperature, we can compare directly the FTS with the experimental results (Fig 6C). The calculated FTS data points under the condition of low salt concentration are shown as filled green squares in Fig 6C.

Next, explicit salt ions were introduced as point charges to simulate an excess salt concentration of 120 mM. We make the assumption that the salt is equally partitioned in both phases, and thus the concentration of salt is a constant, allowing us to sweep the polymer concentration at fixed salt concentration to find the phase coexistence points. A more detailed

449 FTS study of salt partitioning performed using a Gibbs ensemble method found that under
450 conditions of nearly charge-balanced polymers, as is the case in the system of this study, the salts
451 are nearly equipartitioned and counterion condensation is not a dominant factor [67]. Simulations
452 performed in this manner with explicit salt are shown as open green squares in Fig 6C. The FTS
453 data clearly demonstrate that the effect of added salt is to stabilize the single solution phase, and
454 to raise the binodal closer to physiological temperature 37 °C, in agreement with experiments
455 (filled red and blue circles Fig 6C). The complementary dense branch of the binodal curve is also
456 predicted from FTS and is shown in Fig. S11.

457 **Application to cell-complex coacervate co-culture**

458 Looking at the experimental and calculated phase diagrams (Fig 2B, 2C), it is seen that
459 under physiological conditions (T_{cp} ~ 37 °C, [NaCl] ~ 100 mM) it is principally feasible for cells
460 to tune the formation of tau-RNA CCs. This has important implications for studying the
461 physiological roles of tau-RNA CCs, and thus we asked if tau-RNA CCs could indeed exist in a
462 biologically relevant media in the presence of living cells. Both the FH-VO theory and FTS
463 predict that the conditions of high protein concentration, low ionic strength, high temperature
464 and high crowding reagents (acting to lower the excluded volume) would independently favor
465 tau-RNA CC formation. Using these tuning parameters as a guide, we designed several
466 experiments to test the ability for tau-RNA CCs to form in a co-culture with H4 neuroglioma
467 cells. We incubated H4 cells with tau187/tau114-RNA under CC conditions at varying
468 temperatures, polymer concentrations and crowding reagent concentrations. At low polymer
469 concentrations (10 μM tau, 30 μg/ml RNA) no LLPS was observed in the cellular media (Fig 7,
470 first column), where increasing the temperature to 37 °C did not apparently influence the
471 solution phase (Fig 7, first column, first and third row). However, when tau and RNA
472 concentrations were increased (100 μM tau, 300 μg/ml RNA) LLPS could be observed (Fig 7,

second column). Further, LLPS could also be achieved by adding an additional crowding reagent (here PEG) to low concentration samples of tau and RNA (Fig 7, third column). As predicted, LLPS of tau-RNA CC was modulated by (i) temperature, (ii) tau and RNA concentration and/or (iii) the presence of crowding reagent PEG (Fig 7). Lowering the temperature to 18°C significantly reduced the number and size of fluorescent droplets, demonstrating that tau-RNA LLPS is indeed tunable by temperature, and demonstrate the biological consequence of the LCST behavior (Fig 7, first and third row). These results were consistently found for both tau187 and tau114 systems. The successful application of FTS for tuning and predicting tau-RNA CCs in cellular media is a first step towards understanding the physiological condition under which tau-RNA LLPS, which follows the CC mechanism, can occur. The conditions described for LLPS here suggests that conditions exist *in vivo* under which LLPS by complex coacervation may be achieved.

Discussion

The ability of tau to undergo LLPS via a mechanism of complex coacervation has been recognized in a number of recent publications [21,25] [22]. However, to date, the criteria and physical parameters (specifically, polymer concentration, ionic strength, temperature and crowding reagents) that drive tau-RNA CC has not been rationalized. In this paper, we mapped out the experimental phase diagram for tau-RNA CC, and used theory and simulation to describe the parameter space for LLPS. In what follows, we discuss the relevance of our findings in the context of the physical mechanism of LLPS *in vivo.*

Although the FH-VO model cannot model spatially varying charges along the peptide backbone, we were able to fit the experimental data by treating the Flory-Huggins χ parameter as an empirical, temperature-dependent, adjustable parameter. This result highlights the fact that the

FH-VO model is adaptable to experimental data. Still, the FH-VO model has limited predictability, and should be seen as a qualitative descriptor of phase separation. In contrast, FTS is an approximation-free analysis that can provide physical insight and predictive information for biopolymers, such as scaling relationships and polymer or protein sequence effects. As shown above, the tau-RNA phase diagram was successfully reproduced by FTS using model parameters that are reasonable estimates of the experimental physical conditions.With reasonable estimates for the parameters in our polymer model ($\epsilon_r = 80$, $b = 4$ Å), our simulations predict that the lower phase boundary falls in the vicinity of physiological conditions. This finding suggests that FTS can be a powerful theoretical modeling technique to describe and rationalize tau-RNA CC as a competition between short-ranged excluded volume interactions and long-ranged electrostatic interactions.

Consider that we can partition the driving forces of CC as

$$\Delta G^{CC} = \underbrace{\Delta H^{tau/RNA}}_{(-)} - \underbrace{T\Delta S^{comb}}_{(-)} + \underbrace{\Delta H^{ex} - T\Delta S^{noncomb}}_{excluded\ volume\ or\ \chi}$$

where the first two terms are the negative (favorable) enthalpic contribution from tau/RNA interactions and the ideal entropy of mixing term (which is negative because we are considering CC formation). These first two terms are approximately accounted for in the original VO model, and by themselves predict UCST behavior (see SI). The last two terms introduce an non-ionic excess enthalpic contribution and a nonideal, noncombinatoric entropy that are introduced into the FH-VO model through the Flory-Huggins χ parameter, or within FTS through the temperature dependent excluded volume. Given the experimental observation of LCST phase behavior, these terms must be important and we now estimate their value from our model.

Modeling the LCST experimental tau-RNA CC phase diagram using the FH-VO model by invoking an entropic term in the Flory-Huggins χ parameter, or by FTS using a temperature

518 dependent excluded volume, both provide an estimate of the entropic contribution that drives CC
519 formation. The temperature-dependent excluded volume v used to describe LCST phase behavior
520 within FTS can be formally related to the Flory-Huggins χ parameter to second order in the
521 polymer volume fractions $v = b^3(1 - 2\chi)$ [68]. Substituting our empirical excluded volume, we
522 obtain from FTS an interaction parameter χ of the form $\chi = \epsilon_s + \epsilon_H/T$, with ϵ_s being a non-
523 combinatoric entropic term and ϵ_H an enthalpic term. Introducing conventional units (see SI
524 methods for details) gives an unfavorable non-electrostatic enthalpy of phase separation of ΔH^{ex}
525 = 0.23 kJ • mol^{-1} of monomer, and a favorable noncombinatoric entropy of phase separation of
526 $T\Delta S^{noncomb}$ = 1.1 kJ • mol^{-1} of monomer at T = 300 K. For comparison, the empirical χ from
527 fitting the experimental data with the FH-VO model gives ΔH^{ex} = 2.3 kJ • mol^{-1} of monomer and
528 $T\Delta S^{noncomb}$ = 3.24 kJ • mol^{-1} of monomer.

529 Notably, ΔH^{ex} is small and positive. We hypothesize that the positive, i.e. nonionic,
530 enthalpy value for forming a coacervate phase is due to the requirement of breaking favorable
531 interactions between hydrophilic residues and water that stabilizes the solution phase of tau
532 ($\Delta H^{ex} = -\Delta H^{tau/water}$). For comparison, the enthalpy of forming a hydrogen bond ΔH_{HB} at room
533 temperature is ~ −8 kJ • mol^{-1} [69] while the enthalpy of hydration for a polar amino acid ΔH_{hyd}
534 is ~ −60 kJ • mol^{-1} [70,71]. Given that $\Delta H^{tau/RNA}$ for tau–RNA association is negative and tau
535 remains hydrated in the CC state (i.e. tau-water interface is not dehydrated), there has to be a
536 source of penalty in the form of a positive ΔH^{ex} value; the unfavorable ΔH^{ex} associated with tau-
537 RNA CC might come from the loss of hydrogen bonds in the hydration shell from overlapping
538 and sharing of the tau hydration shells in the dense CC phase.

539 The $T\Delta S^{noncomb}$ value is also small, positive and of comparable magnitude as ΔH^{ex}, making
540 temperature increase a facile modulator favoring tau-RNA CC. Given the positive value of ΔH^{ex}

for tau-RNC CC, the entropy gain upon phase separation is contributing to the driving force of tau-RNA CC formation (besides the electrostatic correlation energy between the polycationic and polyanionic polymer segments that is the major driving force). Looking to potential origins for positive $T\Delta S^{noncomb}$, we consider the entropy gain of breaking a hydrogen bond of $T\Delta S_{HB} \sim 6$ kJ • mol^{-1} [69] and the entropy gain associated with the release of a single water molecule from a hydrated surface of ~ 7.5 kJ • mol^{-1} [72]. Given that our FTS study only considered excess ions, but no counterions, while fully capturing the LCST behavior through the excluded volume, *v*, our results are consistent with the hypothesis that competing hydrophilic/hydrophobic interactions are responsible for the LCST behavior [73–75]. At low temperatures, the attractive interaction between water and hydrophilic residues of the biopolymer stabilize the homogenous phase, but above a critical temperature hydrophobic interactions become dominant, in that it becomes more favorable for water to be released from the polymer surface and hydration shell, and for tau and RNA to associate. In this scenario, the entropy gain comes from the release of bound water into the bulk [70] due to overlapping of the hydration shell of tau upon CC. In the literature, the entropy gain of counter ion release [76–79] or compressibility effects [80,81] have been proposed as origins for the LCST behavior, and as prevalent driving forces for CC [82]. While this study cannot entirely delineate between these possible contributions that are all subsumed into the Flory-Huggins χ parameter or the excluded volume parameter in FTS, we demonstrate that it is not necessary to invoke a specific mechanism, such as counter ion release—the most popular hypothesis, to rationalize LCST driven CC formation. In fact, we performed FTS studies with (and without) explicit excess ions (Figure 6C) observing LCST behavior simply by means of excluded volume and electrostatic considerations and not invoking any counter ion release mechanism to capture the phase diagram of the entropy driven tau-RNA CC. Instead, many

564 factors that globally modulate the excluded volume effects in the biological system of interest
565 and that inevitably modulate the hydration water population, including the hydrophobic effect
566 and crowding, may be considered.

567 We demonstrated here that tau-RNA CC can be modeled as a coarse-grained
568 polyelectrolyte mixture using equilibrium theory, and revealed the associated driving factors and
569 the different thermodynamic contributions to the phase diagram. However, this finding does not
570 contradict the possibility that tau-RNA complex coacervation is followed by, or even can
571 facilitate, amyloid fibrillization of tau. Comparing our study to previous reports in the literature
572 [21–23,25,83,84], it is clear that tau in fibrils possess dramatically different properties than tau in
573 CCs. In contrast to fibrils, tau-RNA CCs are reversible and tau remains conformationally
574 dynamic – this is because CCs are formed with a stable tau variant, such as the WT derived tau
575 studied here. However, once aggregation-promoting factors are introduced, not only can the
576 thermodynamically stable phase of tau-RNA CC be driven out of equilibrium, but the dense CC
577 phase harboring high tau and RNA concentration may also lower the activation barrier for, and
578 thus facilitate, tau aggregation. Still, tau complex coacervation is a distinct state and fibrilization
579 is a distinct process, where the equilibrium of one does not contradict with its kinetic
580 transformation into the other. Recently, the possibility of the transformation of tau CCs into tau
581 fibrils has been demonstrated [21]. We have independently investigated these questions and find
582 that irreversible transformation can be triggered by doping tau-RNA CC with highly sulfated
583 polysaccharide heparin (Fig. S12). Tau is first driven towards an equilibrium complex coacervate
584 state, from which tau can either re-dissolve into solution state reversibly, or form amyloid fibrils
585 when aggregation driving force is present. However, the mechanism by which the CC state of tau

586 influences the rate of aggregation and/or alters the aggregation propensity of tau is not
587 understood, and will and should be the subject of future studies.

588 The physiological role of tau-RNA CC as a possible regulatory mechanism or as an
589 intermediate toward fibrilization is an ongoing topic of research. In either case, for tau-RNA CC
590 to be relevant for cellular function LLPS would have to be possible near (certain) physiological
591 conditions. Our *in vitro* experiments found the tau-RNA CC phase diagram boundary to lie near
592 physiological conditions. This suggests that tau-RNA CC can occur *in vivo* upon modulation of
593 parameters, such as the local temperature, electrostatic balance, including local pH, and osmotic
594 pressure. We demonstrate that indeed tau-RNA CC can be achieved in co-culture with living
595 cells. While the coexistence of tau and RNA at low (10 μM) polymer concentrations is not
596 sufficient to drive CC in cellular media, the addition of a molecular crowding reagent is, under
597 physiological conditions (Fig 7). While in this study crowding has been simulated with PEG,
598 many cellular proteins can act as molecular crowding reagents. This data encourages us to
599 speculate that mechanisms that increase the already high concentrations of free proteins and
600 other macromolecular constituents, *not* participating in CC, beyond the normal level within the
601 cell (estimates of 50-200 mg/mL [85]) could be sufficient to promote tau-RNA CC by exerting
602 crowding pressure. Thus, biological mechanisms that increase the concentration of intrinsically
603 disordered and charged proteins and nucleic acids may be potent factors that drive liquid-liquid
604 phase separation in the cellular context. Specifically for the context of this study, high
605 concentrations of tau-RNA are by themselves sufficient to drive CC formation (Fig 7). Given
606 that tau is known to bind and localize to microtubules in the axons of neurons, it is not a stretch
607 to envision a scenario where the local concentration of tau would be highly elevated under
608 certain stress conditions, around regions like the axon initial segment. We proposed at these

609 places in neuron, tau-RNA CCs have a higher probability to be observed. However, even though
610 our calculations and experimental data support a model where tau-RNA CC *in vivo* is possible,
611 whether this actually occurs within the cell depends on many other factors, among them the
612 strength of tau-microtubule binding that compete with tau-RNA CC.
613

614 # Conclusion

615 We report here the first detailed picture of the thermodynamics of tau/RNA complex
616 coacervation. The observation of an LCST phase diagram implies that although electrostatic
617 interactions are key to CC formation, factors that contribute to solvation entropy gain are key to
618 driving liquid-liquid phase separation. We have computed the first approximation-free
619 theoretical phase diagram for tau/RNA complex coacervation from FTS, where we introduced a
620 temperature-dependent excluded volume term. Simulations show a competition between
621 electrostatic strength (parameterized by the salt concentration) and excluded volume
622 (parameterized by the solvent quality). This knowledge can be used to design experiments that
623 perturb this parameter space *in vivo*, as well as predict or understand biological mechanisms that
624 may be favorable towards liquid-liquid phase separation. As a proof of this concept we have
625 shown that by deliberately changing salt concentration, temperature, and solvent quality (by the
626 addition of PEG), we can make tau/RNA LLPS appear or disappear in cellular medium with *live*
627 cells. Interestingly, we find that without any adjustable parameters our simulations predict that
628 tau/RNA is positioned near the binodal phase boundary around physiological conditions. This
629 suggests that small and subtle changes within the cellular environment may be sufficient to
630 induce LLPS in otherwise healthy neurons. Even if the conditions that induce LLPS in the cell is
631 transient, the LLPS state can facilitate irreversible protein aggregation if aggregation-promoting

632 factors are already available, giving credence to the idea that LLPS may play a role in
633 neurodegenerative diseases. However, we speculate that LLPS is reversible in the majority of
634 biological events that drive LLPS, making it hard to observe this state within the cellular context.
635

636 ## Acknowledgement

637 We acknowledge insightful and sustained discussions with Dr. Xumei Zhang on LLPS of tau
638 under cellular conditions. JM would like to thank Scott P.O. Danielsen for helpful discussions
639 regarding FTS. The authors acknowledge the National Institutes of Health (NIH)
640 http://www.nih.gov (grant number R01AG05605) received by SH and KSK and the Tau
641 consortium http://www.tauconsortium.org received by KSK and SH. The funder had no role in
642 study design, data collection and analysis, decision to publish, or preparation of the manuscript.
643 JS acknowledges support from the NSF (MCB-1716956). We acknowledge support from the
644 Center for Scientific Computing from the CNSI, MRL: an NSF MRSEC (DMR-1720256). This
645 work was partially supported by the MRSEC Program of the National Science Foundation under
646 Award No. DMR 1720256.
647
648

REFERENCE

[1] Burke KA, Janke AM, Rhine CL, Fawzi NL. Residue-by-Residue View of In Vitro FUS Granules that Bind the C-Terminal Domain of RNA Polymerase II. Mol Cell. 2015 Oct 15;60(2):231–41.

[2] Brady JP, Farber PJ, Sekhar A, Lin Y-H, Huang R, Bah A, et al. Structural and hydrodynamic properties of an intrinsically disordered region of a germ cell-specific protein on phase separation. Proc Natl Acad Sci. 2017 Sep 26;114(39):E8194–203.

[3] Anderson P, Kedersha N. RNA granules. J Cell Biol. 2006 Mar 13;172(6):803–8.

[4] Brangwynne CP, Eckmann CR, Courson DS, Rybarska A, Hoege C, Gharakhani J, et al. Germline P granules are liquid droplets that localize by controlled dissolution/condensation. Science. 2009 Jun 26;324(5935):1729–32.

[5] Wippich F, Bodenmiller B, Trajkovska MG, Wanka S, Aebersold R, Pelkmans L. Dual specificity kinase DYRK3 couples stress granule condensation/dissolution to mTORC1 signaling. Cell. 2013 Feb 14;152(4):791–805.

[6] Veis A, Aranyi C. Phase separation in polyelectrolyte systems. I. Complex coacervates of gelatin. J Phys Chem. 1960;64(9):1203–1210.

[7] Arneodo C, Baszkin A, Benoit J, Thies C. Interfacial-Tension Behavior of Citrus Oils Against Phases Formed by Complex Coacervation of Gelatin. Acs Symp Ser. 1988;370:132–47.

[8] Water JJ, Schack MM, Velazquez-Campoy A, Maltesen MJ, van de Weert M, Jorgensen L. Complex coacervates of hyaluronic acid and lysozyme: Effect on protein structure and physical stability. Eur J Pharm Biopharm. 2014 Oct;88(2):325–31.

[9] Molliex A, Temirov J, Lee J, Coughlin M, Kanagaraj AP, Kim HJ, et al. Phase Separation by Low Complexity Domains Promotes Stress Granule Assembly and Drives Pathological Fibrillization. Cell. 2015 Sep;163(1):123–33.

[10] Hyman AA, Weber CA, Jülicher F. Liquid-Liquid Phase Separation in Biology. Annu Rev Cell Dev Biol. 2014;30(1):39–58.

[11] Uversky VN, Kuznetsova IM, Turoverov KK, Zaslavsky B. Intrinsically disordered proteins as crucial constituents of cellular aqueous two phase systems and coacervates. FEBS Lett. 2015 Jan 2;589(1):15–22.

[12] Li YR, King OD, Shorter J, Gitler AD. Stress granules as crucibles of ALS pathogenesis. J Cell Biol. 2013 Apr 29;201(3):361–72.

[13] Murakami T, Qamar S, Lin JQ, Schierle GSK, Rees E, Miyashita A, et al. ALS/FTD Mutation-Induced Phase Transition of FUS Liquid Droplets and Reversible Hydrogels into

683 Irreversible Hydrogels Impairs RNP Granule Function. Neuron. 2015 Nov 18;88(4):678–
684 90.

685 [14] Patel A, Lee HO, Jawerth L, Maharana S, Jahnel M, Hein MY, et al. A Liquid-to-Solid
686 Phase Transition of the ALS Protein FUS Accelerated by Disease Mutation. Cell. 2015
687 Aug 27;162(5):1066–77.

688 [15] Kato M, Han TW, Xie S, Shi K, Du X, Wu LC, et al. Cell-free formation of RNA
689 granules: low complexity sequence domains form dynamic fibers within hydrogels. Cell.
690 2012 May 11;149(4):753–67.

691 [16] Li H-R, Chiang W-C, Chou P-C, Wang W-J, Huang J. TAR DNA-binding protein 43
692 (TDP-43) liquid-liquid phase separation is mediated by just a few aromatic residues. J Biol
693 Chem. 2018 Mar 6;jbc.AC117.001037.

694 [17] Kwon I, Xiang S, Kato M, Wu L, Theodoropoulos P, Wang T, et al. Poly-dipeptides
695 encoded by the C9orf72 repeats bind nucleoli, impede RNA biogenesis, and kill cells.
696 Science. 2014 Sep 5;345(6201):1139–45.

697 [18] Lee K-H, Zhang P, Kim HJ, Mitrea DM, Sarkar M, Freibaum BD, et al. C9orf72
698 Dipeptide Repeats Impair the Assembly, Dynamics, and Function of Membrane-Less
699 Organelles. Cell. 2016 Oct 20;167(3):774-788.e17.

700 [19] Boeynaems S, Bogaert E, Kovacs D, Konijnenberg A, Timmerman E, Volkov A, et al.
701 Phase Separation of C9orf72 Dipeptide Repeats Perturbs Stress Granule Dynamics. Mol
702 Cell. 2017 Mar 16;65(6):1044-1055.e5.

703 [20] Nott TJ, Petsalaki E, Farber P, Jervis D, Fussner E, Plochowietz A, et al. Phase Transition
704 of a Disordered Nuage Protein Generates Environmentally Responsive Membraneless
705 Organelles. Mol Cell. 2015 Mar 5;57(5):936–47.

706 [21] Ambadipudi S, Biernat J, Riedel D, Mandelkow E, Zweckstetter M. Liquid–liquid phase
707 separation of the microtubule-binding repeats of the Alzheimer-related protein Tau. Nat
708 Commun. 2017 Aug 17;8(1):275.

709 [22] Zhang X, Lin Y, Eschmann NA, Zhou H, Rauch JN, Hernandez I, et al. RNA stores tau
710 reversibly in complex coacervates. PLOS Biol. 2017 Jul 6;15(7):e2002183.

711 [23] Hernández-Vega A, Braun M, Scharrel L, Jahnel M, Wegmann S, Hyman BT, et al. Local
712 Nucleation of Microtubule Bundles through Tubulin Concentration into a Condensed Tau
713 Phase. Cell Rep. 2017 Sep 5;20(10):2304–12.

714 [24] Ferreon JC, Jain A, Choi K-J, Tsoi PS, MacKenzie KR, Jung SY, et al. Acetylation
715 Disfavors Tau Phase Separation. Int J Mol Sci. 2018 May 4;19(5).

716 [25] Wegmann S, Eftekharzadeh B, Tepper K, Zoltowska KM, Bennett RE, Dujardin S, et al.
717 Tau protein liquid-liquid phase separation can initiate tau aggregation. EMBO J. 2018 Apr
718 3;37(7).

719 [26] Bungenberg de Jong H. Crystallisation–coacervation–flocculation. Colloid Sci.
720 1949;2:232–58.

721 [27] Sing CE. Development of the modern theory of polymeric complex coacervation. Adv
722 Colloid Interface Sci. 2017 Jan;239:2–16.

723 [28] Flory PJ. Principles of Polymer Chemistry [Internet]. 1953 [cited 2018 Jun 21]. Available
724 from: http://archive.org/details/FloryF.1953PrinciplesOfPolymerChemistry

725 [29] Spruijt E, Westphal AH, Borst JW, Cohen Stuart MA, van der Gucht J. Binodal
726 Compositions of Polyelectrolyte Complexes. Macromolecules. 2010 Aug 10;43(15):6476–
727 84.

728 [30] Overbeek JTG, Voorn MJ. Phase separation in polyelectrolyte solutions. Theory of
729 complex coacervation. J Cell Comp Physiol. 1957 May 1;49(S1):7–26.

730 [31] Tainaka K. Study of Complex Coacervation in Low Concentration by Virial Expansion
731 Method. I. Salt Free Systems. J Phys Soc Jpn. 1979 Jun 15;46(6):1899–906.

732 [32] Veis A. PHASE SEPARATION IN POLYELECTROLYTE SYSTEMS. III. EFFECT OF
733 AGGREGATION AND MOLECULAR WEIGHT HETEROGENEITY. J Phys Chem.
734 1963 Oct 1;67(10):1960–4.

735 [33] Tainaka K-I. Effect of counterions on complex coacervation. Biopolymers. 1980 Jul
736 1;19(7):1289–98.

737 [34] Nakajima A, Sato H. Phase relationships of an equivalent mixture of sulfated polyvinyl
738 alcohol and aminoacetalyzed polyvinyl alcohol in microsalt aqueous solution.
739 Biopolymers. 11(7):1345–55.

740 [35] Borue VY, Erukhimovich IY. A statistical theory of weakly charged polyelectrolytes:
741 fluctuations, equation of state and microphase separation. Macromolecules. 1988 Nov
742 1;21(11):3240–9.

743 [36] Borue VY, Erukhimovich IY. A statistical theory of globular polyelectrolyte complexes.
744 Macromolecules. 1990 Jul 1;23(15):3625–32.

745 [37] Castelnovo M, Joanny J-F. Complexation between oppositely charged polyelectrolytes:
746 Beyond the Random Phase Approximation. Eur Phys J E. 2001 Dec 1;6(1):377–86.

747 [38] Biesheuvel PM, Cohen Stuart MA. Electrostatic Free Energy of Weakly Charged
748 Macromolecules in Solution and Intermacromolecular Complexes Consisting of
749 Oppositely Charged Polymers. Langmuir. 2004 Mar 1;20(7):2785–91.

750 [39] Biesheuvel PM, Cohen Stuart MA. Cylindrical Cell Model for the Electrostatic Free
751 Energy of Polyelectrolyte Complexes. Langmuir. 2004 May 1;20(11):4764–70.

[40] Lytle TK, Sing CE. Transfer matrix theory of polymer complex coacervation. Soft Matter. 2017 Oct 11;13(39):7001–12.

[41] Shen K, Wang Z-G. Polyelectrolyte Chain Structure and Solution Phase Behavior. Macromolecules. 2018 Mar 13;51(5):1706–17.

[42] Shen K, Wang Z-G. Electrostatic correlations and the polyelectrolyte self energy. J Chem Phys. 2017 Feb 23;146(8):084901.

[43] Chollakup R, Smitthipong W, Eisenbach CD, Tirrell M. Phase Behavior and Coacervation of Aqueous Poly(acrylic acid)−Poly(allylamine) Solutions. Macromolecules. 2010 Mar 9;43(5):2518–28.

[44] Zalusky AS, Olayo-Valles R, Wolf JH, Hillmyer MA. Ordered Nanoporous Polymers from Polystyrene−Polylactide Block Copolymers. J Am Chem Soc. 2002 Oct 1;124(43):12761–73.

[45] Li L, Srivastava S, Andreev M, Marciel AB, de Pablo JJ, Tirrell MV. Phase Behavior and Salt Partitioning in Polyelectrolyte Complex Coacervates. Macromolecules. 2018 Apr 24;51(8):2988–95.

[46] de la Cruz MO, Belloni L, Delsanti M, Dalbiez JP, Spalla O, Drifford M. Precipitation of highly charged polyelectrolyte solutions in the presence of multivalent salts. J Chem Phys. 1995 Oct 1;103(13):5781–91.

[47] Banjade S, Rosen MK. Phase transitions of multivalent proteins can promote clustering of membrane receptors. eLife. 2014 Oct 16;3:e04123.

[48] Banjade S, Wu Q, Mittal A, Peeples WB, Pappu RV, Rosen MK. Conserved interdomain linker promotes phase separation of the multivalent adaptor protein Nck. Proc Natl Acad Sci. 2015 Nov 24;112(47):E6426–35.

[49] Qin J, de Pablo JJ. Criticality and Connectivity in Macromolecular Charge Complexation. Macromolecules. 2016 Nov 22;49(22):8789–800.

[50] Kudlay A, Olvera de la Cruz M. Precipitation of oppositely charged polyelectrolytes in salt solutions. J Chem Phys. 2003 Dec 23;120(1):404–12.

[51] Kudlay A, Ermoshkin AV, Olvera de la Cruz M. Complexation of Oppositely Charged Polyelectrolytes: Effect of Ion Pair Formation. Macromolecules. 2004 Nov 1;37(24):9231–41.

[52] Castelnovo M, Joanny J-F. Formation of Polyelectrolyte Multilayers. Langmuir. 2000 Sep 1;16(19):7524–32.

[53] Lin Y-H, Song J, Forman-Kay JD, Chan HS. Random-phase-approximation theory for sequence-dependent, biologically functional liquid-liquid phase separation of intrinsically disordered proteins. J Mol Liq. 2017 Feb 1;228:176–93.

787 [54] Lin Y-H, Forman-Kay JD, Chan HS. Sequence-Specific Polyampholyte Phase Separation
788 in Membraneless Organelles. Phys Rev Lett. 2016 Oct 17;117(17):178101.

789 [55] Delaney KT, Fredrickson GH. Theory of polyelectrolyte complexation—Complex
790 coacervates are self-coacervates. J Chem Phys. 2017 Jun 14;146(22):224902.

791 [56] Das S, Eisen A, Lin Y-H, Chan HS. A Lattice Model of Charge-Pattern-Dependent
792 Polyampholyte Phase Separation. J Phys Chem B. 2018 May 31;122(21):5418–31.

793 [57] Peterson DW, Zhou H, Dahlquist FW, Lew J. A soluble oligomer of tau associated with
794 fiber formation analyzed by NMR. Biochemistry. 2008 Jul 15;47(28):7393–404.

795 [58] Gustke N, Trinczek B, Biernat J, Mandelkow E-M, Mandelkow E. Domains of tau Protein
796 and Interactions with Microtubules. Biochemistry. 1994 Oct 16;33(32):9511–22.

797 [59] Siow KS, Delmas G, Patterson D. Cloud-point curves in polymer solutions with adjacent
798 upper and lower critical solution temperatures. Macromolecules. 1972;5(1):29–34.

799 [60] Berry J, Weber SC, Vaidya N, Haataja M, Brangwynne CP. RNA transcription modulates
800 phase transition-driven nuclear body assembly. Proc Natl Acad Sci. 2015 Sep
801 22;112(38):E5237–45.

802 [61] Brangwynne CP, Tompa P, Pappu RV. Polymer physics of intracellular phase transitions.
803 Nat Phys. 2015 Nov;11(11):899–904.

804 [62] Doi M, Edwards SF. The Theory of Polymer Dynamics. Clarendon Press; 1988. 420 p.

805 [63] Stockmayer WH. Chain dimensions near the flory temperature. J Polym Sci. 15(80):595–
806 8.

807 [64] Rubinstein M, Colby RH. Polymer Physics. OUP Oxford; 2003. 458 p.

808 [65] Suzuki H, Ohno K, Inagaki H. An estimation of the temperature dependence of the
809 excluded-volume integral. Eur Polym J. 1982 Jan 1;18(3):247–55.

810 [66] Bianconi A, Ciasca G, Tenenbaum A, Battisti A, Campi G. Temperature and solvent
811 dependence of the dynamical landscape of tau protein conformations. J Biol Phys. 2012
812 Jan 1;38(1):169–79.

813 [67] Danielsen SPO, McCarty J, Shea J-E, Delaney KT, Fredrickson GH. Small Ion Effects on
814 Self-Coacervation Phenomena in Block Polyampholytes. Manuscr Prep. 2018;

815 [68] Gennes P-G de, Gennes PP-G. Scaling Concepts in Polymer Physics. Cornell University
816 Press; 1979. 336 p.

817 [69] Silverstein KAT, Haymet ADJ, Dill KA. The Strength of Hydrogen Bonds in Liquid
818 Water and Around Nonpolar Solutes. J Am Chem Soc. 2000 Aug 23;122(33):8037–41.

[70] Makhatadze GI, Privalov PL. Contribution of Hydration to Protein Folding Thermodynamics: I. The Enthalpy of Hydration. J Mol Biol. 1993 Jul 20;232(2):639–59.

[71] Matubayasi N. Free-energy analysis of protein solvation with all-atom molecular dynamics simulation combined with a theory of solutions. Curr Opin Struct Biol. 2017 Apr 1;43:45–54.

[72] Thirumalai D, Reddy G, Straub JE. Role of Water in Protein Aggregation and Amyloid Polymorphism. Acc Chem Res. 2012 Jan 17;45(1):83–92.

[73] Feil H, Bae YH, Feijen J, Kim SW. Effect of comonomer hydrophilicity and ionization on the lower critical solution temperature of N-isopropylacrylamide copolymers. Macromolecules. 1993 May;26(10):2496–500.

[74] Choi E, Yethiraj A. Entropic Mechanism for the Lower Critical Solution Temperature of Poly(ethylene oxide) in a Room Temperature Ionic Liquid. ACS Macro Lett. 2015 Jul 21;4(7):799–803.

[75] Martin EW, Mittag T. Relationship of Sequence and Phase Separation in Protein Low-Complexity Regions. Biochemistry. 2018 01;57(17):2478–87.

[76] Dobrynin AV, Rubinstein M. Counterion Condensation and Phase Separation in Solutions of Hydrophobic Polyelectrolytes. Macromolecules. 2001 Mar 1;34(6):1964–72.

[77] Gummel J, Cousin F, Boué F. Counterions Release from Electrostatic Complexes of Polyelectrolytes and Proteins of Opposite Charge: A Direct Measurement. J Am Chem Soc. 2007 May 1;129(18):5806–7.

[78] Muthukumar M. Theory of counter-ion condensation on flexible polyelectrolytes: Adsorption mechanism. J Chem Phys. 2004 Apr 29;120(19):9343–50.

[79] Hone JHE, Howe AM, Cosgrove T. A Small-Angle Neutron Scattering Study of the Structure of Gelatin/Polyelectrolyte Complexes. Macromolecules. 2000 Feb 1;33(4):1206–12.

[80] Lacombe RH, Sanchez IC. Statistical thermodynamics of fluid mixtures. J Phys Chem. 1976 Nov 1;80(23):2568–80.

[81] Sanchez IC, Lacombe RH. Statistical Thermodynamics of Polymer Solutions. Macromolecules. 1978 Nov 1;11(6):1145–56.

[82] Chang L-W, Lytle TK, Radhakrishna M, Madinya JJ, Vélez J, Sing CE, et al. Sequence and entropy-based control of complex coacervates. Nat Commun. 2017 Nov 2;8(1):1273.

[83] Eschmann NA, Georgieva ER, Ganguly P, Borbat PP, Rappaport MD, Akdogan Y, et al. Signature of an aggregation-prone conformation of tau. Sci Rep. 2017 Mar 17;7:44739.

852 [84] Pavlova A, Cheng C-Y, Kinnebrew M, Lew J, Dahlquist FW, Han S. Protein structural
853 and surface water rearrangement constitute major events in the earliest aggregation stages
854 of tau. Proc Natl Acad Sci. 2016;113(2):E127–E136.

855 [85] Finka A, Goloubinoff P. Proteomic data from human cell cultures refine mechanisms of
856 chaperone-mediated protein homeostasis. Cell Stress Chaperones. 2013 Sep;18(5):591–
857 605.

858

859

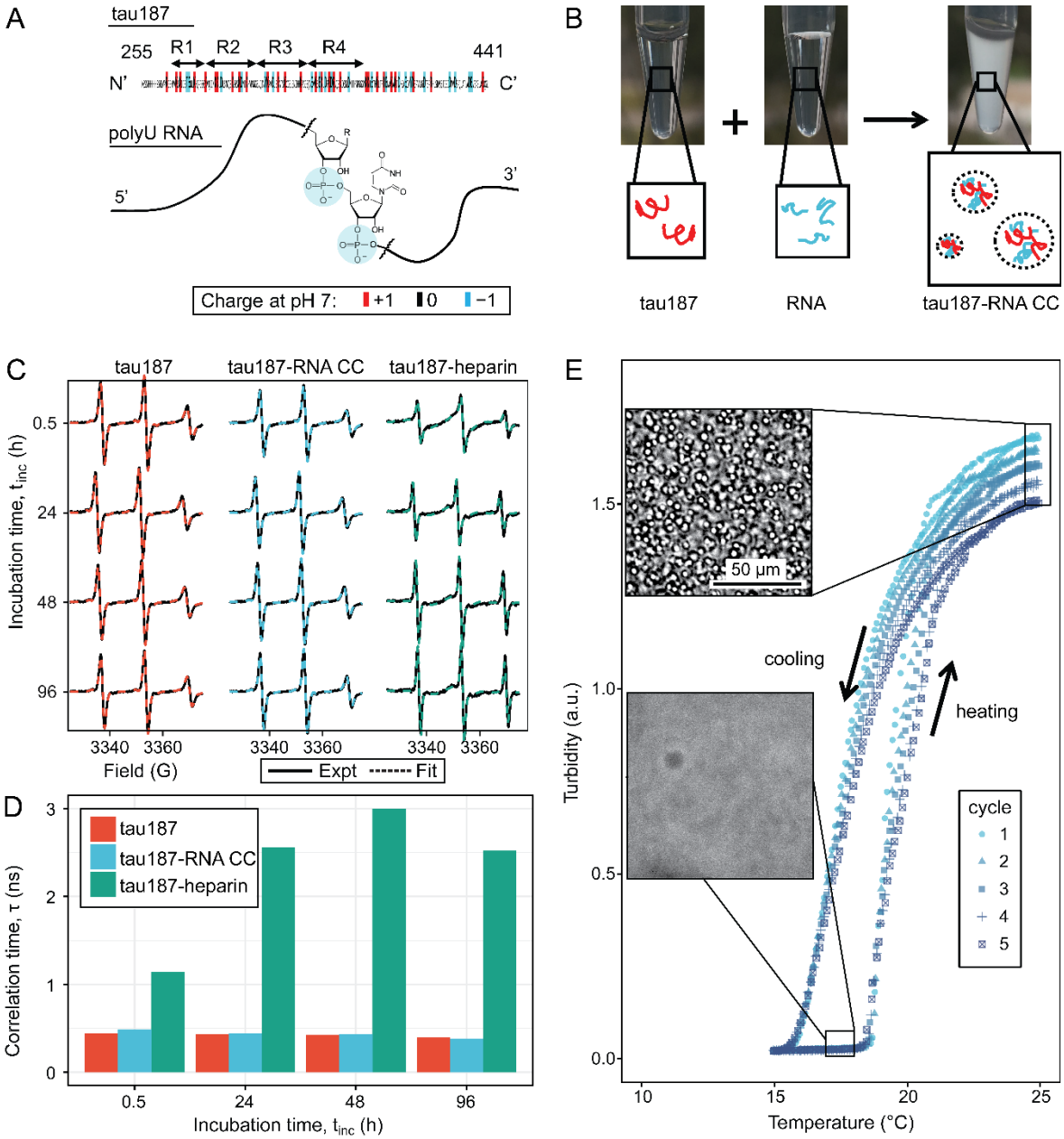

FIG. 1 Steady tau dynamics and reversible droplet formation of tau-RNA complex coacervates. A. Diagram of tau187 (tau) and polyU RNA (RNA). Tau187 is a truncated version of full-length human tau (2N4R 255-441) containing repeat domains and C terminal. At neutral pH experimental conditions, tau187 is overall positively charged; while RNA consists of a phosphate backbone and is negatively charged. **B.** Scheme of tau-RNA CC preparation. Mixing clear tau187 and RNA solutions at proper conditions results in a turbid solution containing liquid

droplets. **C.** X-band cw-EPR spectra (solid line) of tau187 solution (tau187, red), tau187-RNA CC (blue) and tau187-heparin (green) at room temperature with different incubation time, t_{inc}. Samples contains 500 μM tau with 20% spin-labelled. EPR simulation were performed (SI Method) and the fitted spectra is shown as a dashed line. **D.** Rotational correlation time, τ_R extracted from EPR simulation shown in (b1) (SI Method). **E.** Turbidity of tau187-RNA suspension in consecutive heating-cooling cycles. Confocal images represented samples at 19 °C and 25 °C. Temperatures were ramped at 1 °C/min.

FIGURE 2

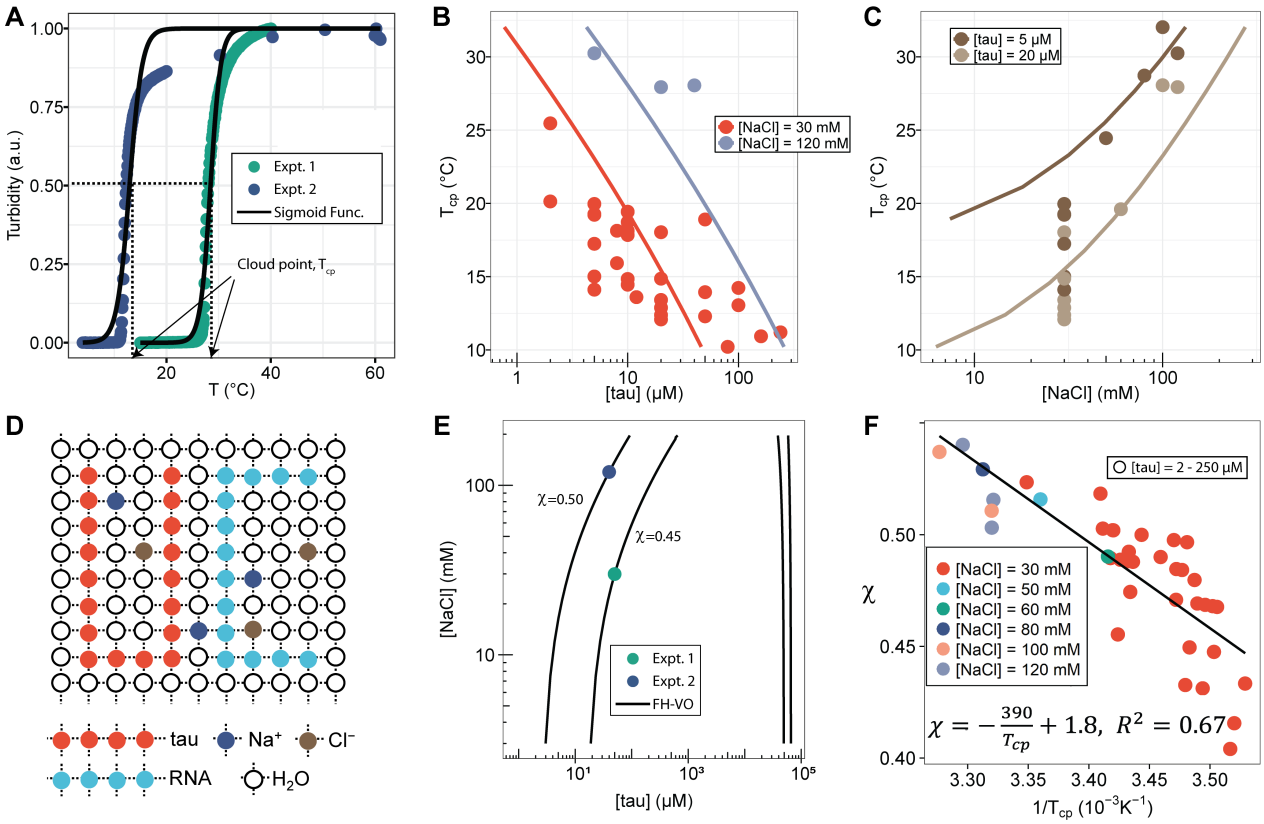

FIG. 2 FH-VO modeling of tau-RNA CC. A. Turbidity of tau187-RNA CC upon heating (Expt.1 ([tau], [NaCl]) = (50 μM, 120 mM), green dots; Expt.2 ([tau], [NaCl]) = (40 μM, 30 mM), purple dots). Absorbance at λ = 500 nm were normalized and used as turbidity value. Turbidity-temperature data of the heating curves were fitted with a sigmoidal function (solid line) as described in (SI Method), and the temperature at which normalized turbidity reaches 0.5 was assigned to cloud point, T_{cp}. **B-C.** Experimental phase diagram (points) showing [tau] vs. T_{cp} and [NaCl] vs. T_{cp} along with the binodal curve generated from fitting the data to the FH-VO model with $\chi = \chi(T_{cp})$ (solid line) **D.** Diagram of Flory Huggins lattice. Tau and RNA are represented by consecutively occupied lattice sites. **E.** Each experimental condition in (**A**) was

independently fit to the FH-VO model (solid lines) to obtain an empirical χ value. **E** shows two representative curves**.** These empirically determined values of χ are shown as points in **F.** The solid line in **F** is a linear regression, generating $\chi = \chi(T_{cp})$, which is then used to generate the binodal lines in **B** and **C**.

FIGURE 3

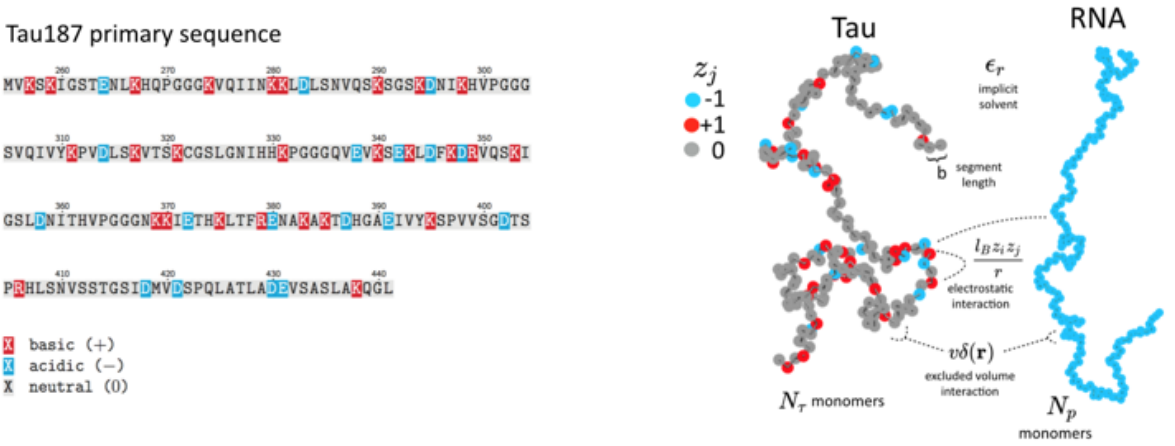

FIG. 3 Schematic depiction of the polyelectrolyte model. Tau and RNA molecules are represented as bead-spring polymers with segment length *b* in implicit solvent. Tau is modeled as a polyampholyte with the charge of each monomer determined from the amino acid charge at pH=7. RNA is modeled as a fully charged polyelectrolyte. In addition to chain connectivity, all monomers interact with an excluded volume repulsive potential, and charged monomers interact with a long-ranged Coulomb potential.

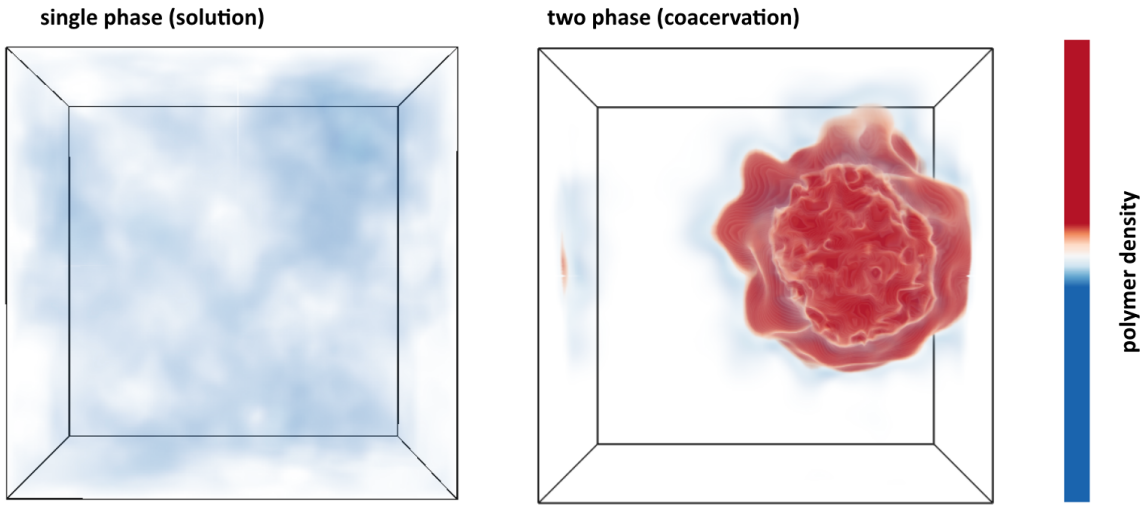

FIG. 4 Polymer density field from FTS. **Left:** Polymer density profile showing a single solution phase for the condition of relatively weak electrostatic strength $l_B = 0.16\ b$ and relatively high excluded volume (good solvent conditions) $v = 0.02\ b^3$. The solution phase is characterized by near homogeneous low polymer density (white/light blue) throughout the entire simulation box. **Right:** Polymer density profile showing complex coacervation upon increasing the electrostatic strength to $l_B = 3.25\ b$ and decreasing the solvent quality by lowering the excluded volume to $v = 0.0068\ b^3$. The two phase region is characterized by a distinct region of high polymer density (dark red) and a surrounding region of low polymer density (white) within the same simulation box. The total polymer concentration is the same in both simulations.

FIGURE 5

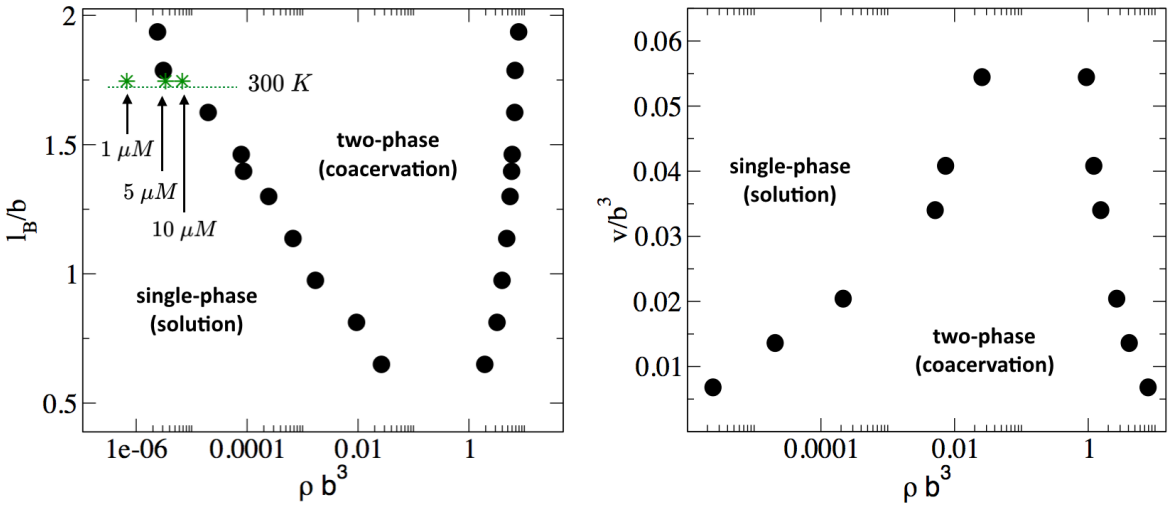

FIG. 5 Phase diagram of the Tau/RNA model obtained from FTS. **(Left)** Binodal points as a function of the Bjerrum length at fixed excluded volume of $v = 0.0068\ b^3$. For comparison three concentrations at 300 K are indicated (arrows) assuming $\epsilon_r = 80$ and $b = 4$ Å **(Right)** Binodal points as a function of the excluded volume at fixed Bjerrum length $l_B = 1.79\ b$

FIGURE 6

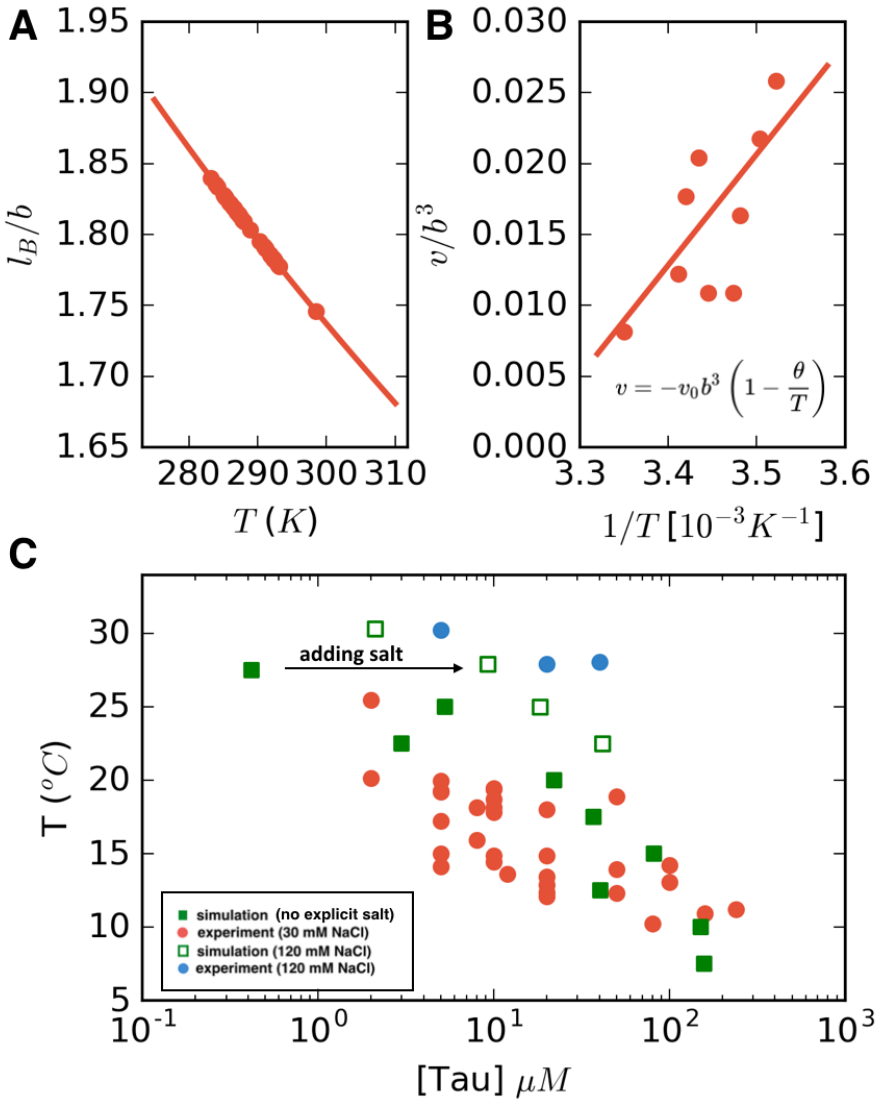

FIG 6 LCST phase behavior from FTS: (**A)** Temperature dependence of the reduced Bjerrum length (ε=80 for water) shown in red. **(B)** Temperature dependence of the excluded volume obtained by adjusting the excluded volume parameter until FTS agrees with a subset of the experimental data (points). The solid line shows a linear fit to the data which is used to obtain the temperature dependent excluded volume for subsequent simulations. **(C)** FTS coexistence points (filled green squares) obtained by using a temperature dependent Bjerrum length (Fig 6A) and excluded volume (Fig 6B). Experiments performed at 20 mM NaCl are shown in red for comparison. Upon introducing excess salt ions in FTS with a fixed

concentration of [NaCl] = 120 mM, the binodal shifts upwards (open green squares). For comparison experiments performed at 120 mM NaCl are shown in blue.

FIGURE 7

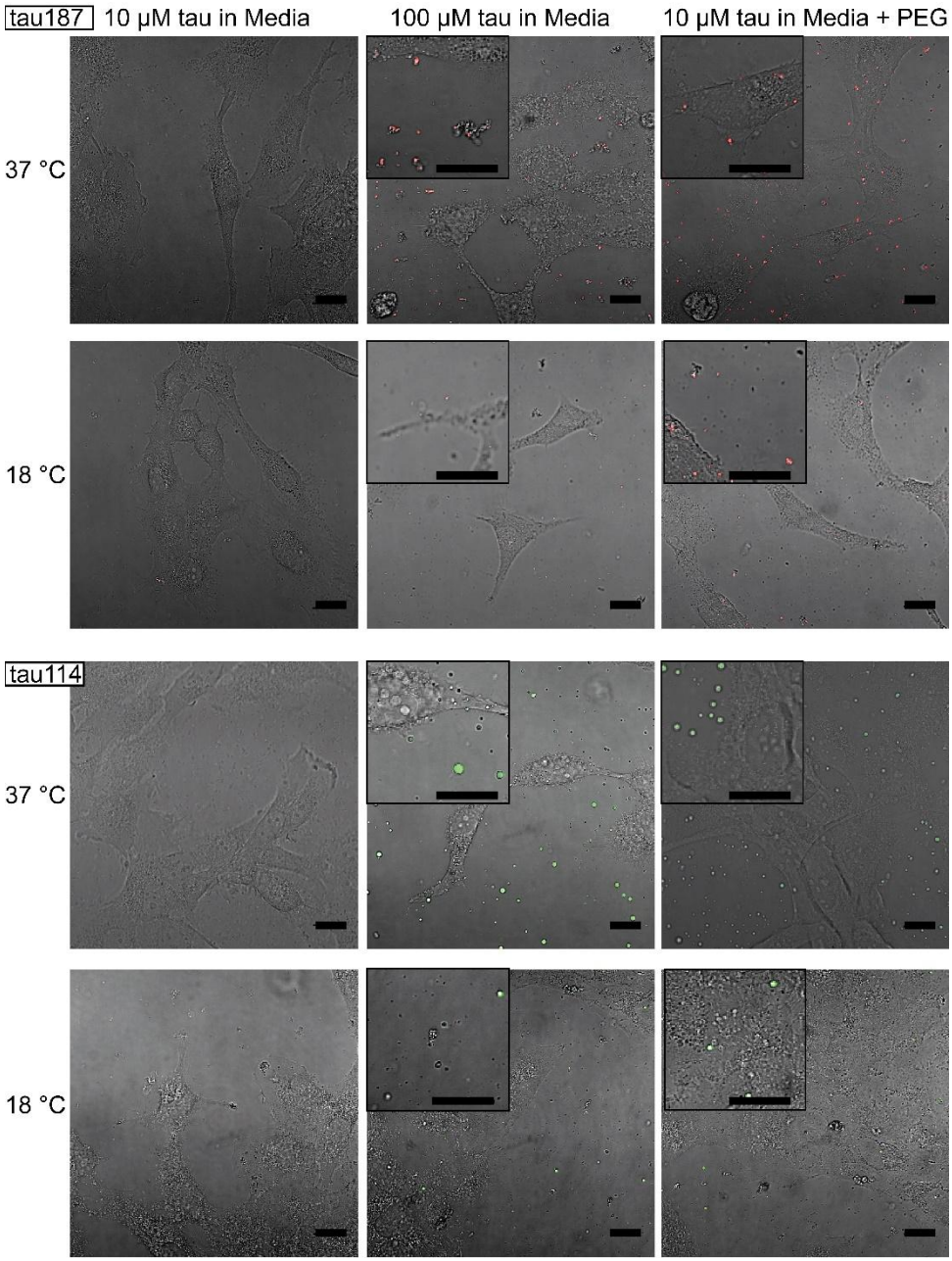

FIG. 7 Tuning experimental conditions to catch tau-RNA complex coacervates in presence of living cells. Bright field images and superimposing fluorescence images of tau-RNA CC coculturing with H4 cells, with 10 μM tau (left), 100 μM tau (middle) and 10 μM tau with 10% v.v. PEG (right). Samples at 37 °C (first row) and 18 °C (second row) were images with

representative images showing the co-presence of living cells and tau-RNA CCs. Tau187 (Top) and tau114 (Bottom) was used showing tau114 with higher propensity at CC formation. Alexa Fluor 488 was used to prepare fluorescent labeled tau. 3 μg/mL polyU RNA per 1 μM tau was used to prepared samples. Scale bar is 20 μm.